Near-infrared Spectroscopy for Remote Sensing of Porosity, Density, and Cubicity of Crystalline and Amorphous H₂O Ices in Astrophysical Environments

Christina M. Tonauer[1] , Eva-Maria Köck[1] , Raphael Henn[2] , Josef N. Stern[1] , Leonardo del Rosso[3] , Milva Celli[3] ,
Christoph Kappacher[2] , Sophia Leiter[2] , Christian G. Kirchler[2] , Christian W. Huck[2] , and Thomas Loerting[1]

[1] Institute of Physical Chemistry, University of Innsbruck, A-6020 Innsbruck, Austria; thomas.loerting@uibk.ac.at
[2] Institute of Analytical Chemistry and Radiochemistry, University of Innsbruck, A-6020 Innsbruck, Austria
[3] Consiglio Nazionale delle Ricerche, Istituto di Fisica Applicata "Nello Carrara", via Madonna del Piano 10, I-50019 Sesto Fiorentino, Italy

Abstract

We present laboratory spectra of pure amorphous and crystalline H₂O ices in the near-infrared (NIR, 1–2.5 μm/ 10,000–4000 cm^{-1}) at 80–180 K. The aim of this study is to provide spectroscopic reference data that allow remotely accessing ice properties for icy objects such as icy moons, cometary ice, or Saturn rings. Specifically, we identify new spectral markers for assessing three important properties of ices in space: (i) porosity/fluffiness, (ii) bulk density of amorphous ice, and (iii) cubicity in crystalline ice. The analysis is based on the first OH-stretching overtone ($2\nu_{OH}$) and the combinational band at 5000 cm^{-1}/2 μm, which are potent spectral markers for these properties. By comparison of vapor-deposited, microporous amorphous solid water, pore-free low-, high-, and very-high-density amorphous ice, we are able to separate the effect of (bulk) density from the effect of porosity on NIR-spectra of amorphous ices. This allows for clarifying a longstanding inconsistency about the density of amorphous ice vapor-deposited at low temperatures, first brought up by Jenniskens & Blake. Direct comparison of NIR spectra with powder X-ray diffractograms allows us to correlate spectral features with the number of cubic stacking layers in stacking-disordered ice I$_{sd}$, ranging from fully cubic ice I$_c$ to fully hexagonal ice I$_h$. We show that exposure times for instruments on the James Webb Space Telescope are in the hour range to distinguish these properties, demonstrating the usefulness of the neglected NIR spectral range for identifying ices in space.

Unified Astronomy Thesaurus concepts: Ice spectroscopy (2250); Ice physics (2228); Spectroscopy (1558); Ice porosity (2274); Ice phases (2273); James Webb Space Telescope (2291); Infrared spectroscopy (2285)

Materials only available in the online version of record: machine-readable tables

1. Introduction

Water is ubiquitous, and its presence, structure, and reactions are universal indicators for the conditions in astronomical surroundings. Water in dense, molecular interstellar clouds at ∼10 K is found as a porous amorphous solid (McClure et al. 2023). While billion-year-old comets in Oort cloud may feature microporous amorphous ices with trapped gases (Alan Stern 2003), comets approaching the Sun may experience a collapse of these pores, outgassing of the trapped species and crystallization (Klinger 1985; Mayer & Pletzer 1986, 1987; Bar-Nun et al. 1987; Hallbrucker & Mayer 1991). At the surface of icy moons such as Europa, Ganymede, or Enceladus, ice is often found as crystalline ice at temperatures near 100 K. In some cases, even liquid water might be encountered (Porco et al. 2006; Robidel et al. 2020). For example, Saturn's moon Enceladus features a surface of mostly pure water ice. Active jets of water vapor and ice grains emanate from the so-called *Tiger Stripes* at the South Pole, as identified by the Cassini mission (Porco et al. 2006; Robidel et al. 2020 and references therein). That is, at the surface of this active body, a variety of structurally different water ices are plausible: (i) plumes of liquid and gaseous water ejected from the cryo-volcanoes, (ii) vitrified water after exposure of gaseous/liquid water to the low surface temperatures (∼70 K) resulting in more or less

porous low-density amorphous ices, supplying Saturn's E-ring but also falling back to the surface as "amorphous snow." Along the warmer regions at the *Tiger Stripes* these ices might crystallize to (iii) ice I. Depending on temperature history, the ice I might be composed of hexagonal stacking sequences (such as snow and ice on Earth) or might also contain cubic stacking sequences. This is known as polytypism of ice I, where three types are distinguished, namely purely cubic, purely hexagonal, and stacking-disordered ice I (ice I$_h$, ice I$_c$; del Rosso et al. 2020; Komatsu et al. 2020) and ice I$_{sd}$ (Kuhs et al. 2012; Malkin et al. 2015). Furthermore, parts of Enceladus show craters up to 35 km in diameter (Bland et al. 2012) formed through impacts or tectonic stress events (Kargel & Pozio 1996). These events are associated with extreme pressure spikes that allow for formation of (iv) high- or even very high-density ices. In the present laboratory near-infrared spectroscopy study, we have prepared analogs of all these abovementioned water ices at ∼80 K, providing new spectroscopic NIR reference data for remote analysis.

That is, water in space forms via various routes, which we mimic in the laboratory directly for the abovementioned examples. A common route observed in space that we do not follow in our laboratory work comprises gas phase reactions of atomic oxygen O with molecular hydrogen H₂, forming an OH species that further reacts with H₂ to H₂O (Harada et al. 2010, 2012). We also do not prepare ices based on surface reactions, which is a common process on dust grains consisting of amorphous silicates and carbonaceous materials in interstellar clouds (Van Dishoeck et al. 2013). Due to its ability to trap

other small molecules, water ice on such dust particles plays a major role as a catalyst for the formation of complex organic molecules in space (Bar-Nun et al. 1987; Öberg 2016). Thus, interstellar dust grains coated with water ice exposed to harsh ionizing radiation are often referred to as "cradles of life." Even though we do not follow the exact same routes of ice formation that are encountered in interstellar clouds, we produce icy materials that might resemble the amorphous ices on these dust grains. Consequently, our laboratory data on astronomical ice analogs such as porous amorphous solid water (pASW) prepared in a lab via vapor deposition (Burton & Oliver 1935; Tonauer et al. 2023a) can be used for understanding reactivity in many astronomical environment as explained above, including dense, interstellar clouds. Yet for understanding ice in interstellar clouds, it would be desirable to study the ice analogs at even lower temperature ($\sim$10 K), where our present study is limited to the range 80–180 K.

For remote detection of porous water ice in space, the vibrational signature of dangling bonds (DB) at the ice/pore surface in the mid-and near-IR range is so far the most utilized approach (Tribbett et al. 2021; McClure et al. 2023). Nevertheless, these features are weak ($\sim$1% of the intensity of bands of (fully) four-coordinated water molecules) and may easily be masked by bands from other species. Furthermore, it has been shown that dangling bond bands are not a fully conclusive measure for porosity, since their disappearance at higher temperatures does exclude remaining pores (Isokoski et al. 2014; Cazaux et al. 2015).

For this reason, more characteristic marker bands for porosity of astronomical water ices in the mid-and near-IR range, based on laboratory work on ice analogs, are desirable. The pores in pASW are known to collapse at temperatures >120 K (Bossa et al. 2012; Mitterdorfer et al. 2014) or upon particle bombardment (Palumbo 2006; Dartois et al. 2013). To study the spectral features of such fully collapsed, pore-free amorphous solid water, so-called "low-density amorphous ice" (LDA) prepared via high-pressure and low-temperature synthesis (Mishima et al. 1985) is a suitable analog. Yet, there is no reference spectrum over the whole near-infrared range (NIR; 1–2.5 μm, 10,000–4000 cm^{-1}) available for LDA.

As mentioned above, based on the example of Enceladus, there is good reason to assume that also other forms of amorphous water ice of higher density might be present in space, e.g., at the surface of larger icy bodies exposed to heavy impacts (Mejía et al. 2015) or bodies with cryo-volcanism, e.g., after events of tectonic stress relief (McBride et al. 2004; Lin et al. 2018). To study such denser H_2O ices in a lab, "high-density amorphous ice" (HDA; Mishima et al. 1984) and "very high-density amorphous ice" (VHDA; Loerting et al. 2001) prepared at low-T/high-p conditions are reasonable model systems for spectroscopic benchmarking experiments. So far, however these polyamorphs have only been studied in a limited spectral range (<5000 cm^{-1}/>2 μm, (LDA, HDA)) (Karina et al. 2022) or not at all (VHDA). Nevertheless, our previous study has revealed that, in particular, the first overtone of the OH-stretching vibration ($2\nu_{OH}$, $\sim$6600 cm^{-1}/$\sim$1.5 μm) is a potent spectral marker for density and thus the different forms of ice (Tonauer et al. 2021).

In light of the idea that vapor deposition at $\sim$15 K might result in high-density ices (Jenniskens & Blake 1994), it is of interest to differentiate between dense and porous ices via infrared spectroscopy. The conclusion by Jenniskens & Blake

that the frost on interstellar grains as well as on Kuiper Belt objects is high-density ice has both been contested (Kolesnikov et al. 1997; Gärtner et al. 2019) and accepted (Baragiola 2003; Burke & Brown 2010; Van Dishoeck et al. 2013) and used to explain irreversible spectral changes upon heating of H_2O vapor deposits (Mastrapa et al. 2008). Without question, it is important to identify the difference between porous and dense ices in the actual sense: Porous water ices are dominated by surfaces and therefore by water molecules that are less coordinated than a fully four-fold coordinated bulk water molecule, acting two times as an H-bond donor and two times as an H-bond acceptor, respectively. Dense, pore-free ices on the other hand, are dominated by bulk water molecules, and depending on the external pressure, their coordination number can increase to 5 (HDA) or even 6 (VHDA; Loerting et al. 2011b). Therefore, disentangling the spectral signatures of porosity and density of ices is of fundamental as well as astrophysical interest.

Another hot topic is the differentiation between crystalline and amorphous ices in space, because it offers clues about the temperature (history) of celestial bodies (Leto et al. 2005) and atmospheric and tectonic processes. Yet, only laboratory spectra of pASW (Mastrapa et al. 2008) and hexagonal ice I_h (Schmitt et al. 1998) were considered for crystallinity models (Berdis et al. 2022). Especially in the temperature range between 140 and 220 K, cubic ice I_c and "stacking-disordered" ice I_{sd} (Kuhs et al. 2012; Malkin et al. 2015) may also appear in space. Since these two "polytypes" of ice I are metastable relative to ice I_h (Tonauer et al. 2023b) the detection of one or the other structure could offer more precise information on thermal history. So far, an IR spectroscopic study on ice I_c in comparison with ice I_h and ice I_{sd} has not been accessible, because pure cubic ice was first experimentally realized only in 2020 (del Rosso et al. 2020; Komatsu et al. 2020).

The launch of James Webb Space Telescope (JWST) marks the dawn of a new age of remote sensing of astronomical objects, and therefore laboratory studies as references for spectra collected from space are needed. In this work, we address the above-mentioned challenges and open questions regarding near-infrared studies of amorphous and crystalline water ices of astronomical interest. Specifically, we here provide NIR spectra in combination with powder X-ray diffraction of the following types of ices: (i) vapor-deposited pASW, (ii) partially collapsed ASW, (iii) pore-free LDA, (iv) HDA, (v) VHDA, (vi) ice I_c, and (vii) ice I_{sd} in comparison with ice I_h. While ices in space typically occur as mixtures of several components and systematic lab studies on multicomponent ices are crucial (Bossa et al. 2015; Terwisscha Van Scheltinga et al. 2021; Rocha et al. 2022), in the present study we focus on ice analogs from pure H_2O. The astronomically relevant issues for pure water that we tackle here are threefold: identification of spectral markers for porosity, for bulk density of amorphous ice, and for the number of cubic stacking faults in crystalline ice I. The observation of three different types of amorphous ice is known as "polyamorphism" (Mishima et al. 1984, 19). The possibility of both hexagonal and cubic stacking sequences in ice I is known as "polytypism" (Malkin et al. 2015). All of the three properties identified in our work are of key astronomical relevance to understand the thermal and/or pressure history of ices in space. The pores in amorphous solid water are known to cluster (Wu et al. 2010; Bossa et al. 2015) before they start to collapse $\sim$120 K (Mitterdorfer et al. 2014). The transition from stacking-disordered ice I_{sd} of high cubicity to hexagonal ice

without any cubicity takes place in the temperature range 150–220 K (Tonauer et al. 2023b). The presence of high-density amorphous ices is only possible if pressures above 1 GPa at temperatures below 180 K persist (Tonauer et al. 2023a). That is, by studying the combination of seven different laboratory ices here, both crystalline and amorphous, we are able to learn a lot about the thermal and pressure history of icy objects in space. Furthermore, this analysis requires a combination of cryo-X-ray-powder diffraction and NIR spectroscopy.

2. Experimental Methods

High-pressure/low-temperature preparations were performed using the established custom-made piston-cylinder setup described in (Tonauer et al. 2018). More specifically, volumes of 400–600 μm of liquid ultrapure H_2O (*Milli-Q*, 18.2 MΩ·cm at 298 K) were filled into indium containers, frozen to hexagonal ice, and inserted into the central 8 mm bore of the cooled piston cylinder cell. Pressure-/temperature-controlled protocols were executed using a commercial "universal material testing machine" (*Zwick*, model *BZ100/TL3S*). Temperature was measured using a Pt-100 temperature sensor and controlled via a *Lakeshore* temperature controller. This experimental setup allows for simultaneous detection and control of piston displacement (corresponding to volume change), temperature (77–300 K), and pressure (up to ~2 GPa). Low-, high- and very high-density amorphous ice (LDA, HDA, and VHDA) were prepared via pressure induced amorphization of hexagonal ice, resulting in (unannealed) high-density amorphous ice at ~1.1 GPa and 77 K (Mishima et al. 1984). Isobaric annealing at 1.1 GPa to 160 K yields VHDA and subsequent decompression to 200 and 2 MPa at 140 K yield (expanded) HDA and LDA, respectively. Ice I_{sd} was made by heating ice V (previously crystallized from ice I_h at 0.5 GPa in that setup) to ~158 K at 2 MPa. Ice I_c was crystallized from ice XVII as described in del Rosso et al. (2020). All of these ices are quench recovered under liquid nitrogen. That is, in every step after preparation (recovery, storage, and spectroscopy) these samples are immersed under liquid nitrogen. During NIR measurements, ice samples are inside cuvettes together with liquid nitrogen. That is, during the time of an NIR scan (typically 15 s), liquid nitrogen evaporates, creating a flow *from* the sample to the surrounding air. Condensation of water from the atmosphere would require a flow *to* the sample, and so the samples are protected from condensation at all times.

pASW was prepared by background vapor deposition in a high-vacuum glass apparatus developed by Mayer & Pletzer (1984; see their Figure 2). More specifically, H_2O vapor (from a reservoir of liquid, ultrapure, and degassed water) was inserted into the chamber at a deposition pressure of $5 \cdot 10^{-1}$ mbar (minimum background pressure: $5 \cdot 10^{-6}$ mbar). We expect a similar ratio of $1:10^5$ of impurities:H_2O in the ASW deposit, where background gas molecules such as N_2 and O_2 might be trapped within the micropores of ASW. Because of the sticking coefficient of the background molecules being quite low on H_2O ice, a significant fraction will actually be reflected after impinging on the ASW deposit. This leads to impurity levels within ASW of ppm and smaller.

In order to allow for background deposition conditions, the flow was baffled before it hit the copper plate, which is cooled to ~80 K by a reservoir of liquid nitrogen (Mayer & Pletzer 1984). This experimental setup allows for deposition rates of

~1 mm hr^{-1} and for recovery of mm-thick pieces of porous amorphous solid water for further analyses. For sample recovery, the chamber is vented with an overpressure of dry, gaseous argon. This allows us to remove the cryoplate from the chamber and immediately immerse it in liquid nitrogen. Thus, this technique avoids exposure of the samples to air, and thereby condensation of water vapor onto the sample can be excluded. After the copper plate with its liquid nitrogen reservoir is taken out of the chamber and put into a bath of liquid nitrogen, the deposit is scratched off the plate while under liquid nitrogen. By weighing a cylindrical pASW deposit of known thickness and diameter, we approximate a density of $\rho \sim 0.4$ g cm^{-3}, corresponding to ~60% porosity (Kimmel et al. 2001; Dohnálek et al. 2003). The identity of every batch was confirmed by powder X-ray diffraction (PXRD) in θ–θ geometry at ~80 K and 1 mbar (Cu-Kα; *Siemens D5000* or *Bruker d8 discover*, see Figure A2). Calorimetric cubicity of ice I_{sd} was determined by differential scanning calorimetry (*DSC8000* by *Perkin Elmer*; Tonauer et al. 2023b). The near-infrared spectroscopy method using a *Büchi NIR Flex N-500* benchtop FT-NIR spectrometer is described in Tonauer et al. (2021). Accordingly, samples were powdered under liquid nitrogen (individual particle sizes ~30–300 μm) and filled into quartz cuvettes. Spectra were collected in diffuse reflectance mode and converted to Kubelka–Munk (K-M) spectra (Kubelka & Munk 1931; Torrent & Barrón 2015). According to Kubelka–Munk theory, the weakening of the incident beam is a result of absorption and scattering processes, where transmission is assumed to be negligible. We ensured this condition by filling at least 1 mm thick powder layers into the cuvette (Tonauer et al. 2021). The resulting Kubelka–Munk function (or remission function) is the ratio between the absorption and scattering coefficient. While diffuse reflectance spectroscopy does not allow for the extraction of absorptivities according to Lambert–Beer's law, the K-M function spectra compare very well with absorbance spectra in literature, e.g., of vapor-deposited amorphous solid water (Mastrapa et al. 2008) or of ice I_h (Grundy & Schmitt 1998) regarding peak positions, relative intensities, and peak broadness (FWHM), backing the use of diffuse reflectance spectroscopy.

For baseline correction, a basis spline constructed from eight anchor points was subtracted from raw spectra (provided in SI). Normalized spectra were then summed up and shown in Figures 1(a), 1(b), 2(a), 2(b), 3(a), and 3(b), scaled to the maximum of the chosen band (100% K-M). The spectrum of Centaur 10199 Chariklo shown in Figures 3(a) and 3(b) was recorded using JWST's Near-Infrared Spectrograph (NIRSpec), in 2022 October and retrieved as a reflectance spectrum from AURA's Space Telescope Science Institute webpage, https://webbtelescope.org/contents/media/images/01GQJ89HXD39F20PSXS2KKKREB, downloaded 2023 March 29, (Pinilla-Alonso et al. 2023), Image credit: NASA, ESA, CSA, Leah Hustak. After conversion from the reflectance to a K-M spectrum, smoothing (adjacent-averaging, points of window: 5) and background correction (using a spline function with five anchor points) was performed.

3. Results and Discussion

3.1. Porosity

Figures 1(a) and (b) show the two main features in the NIR spectra of pASW, partially collapsed ASW, nonporous LDA,
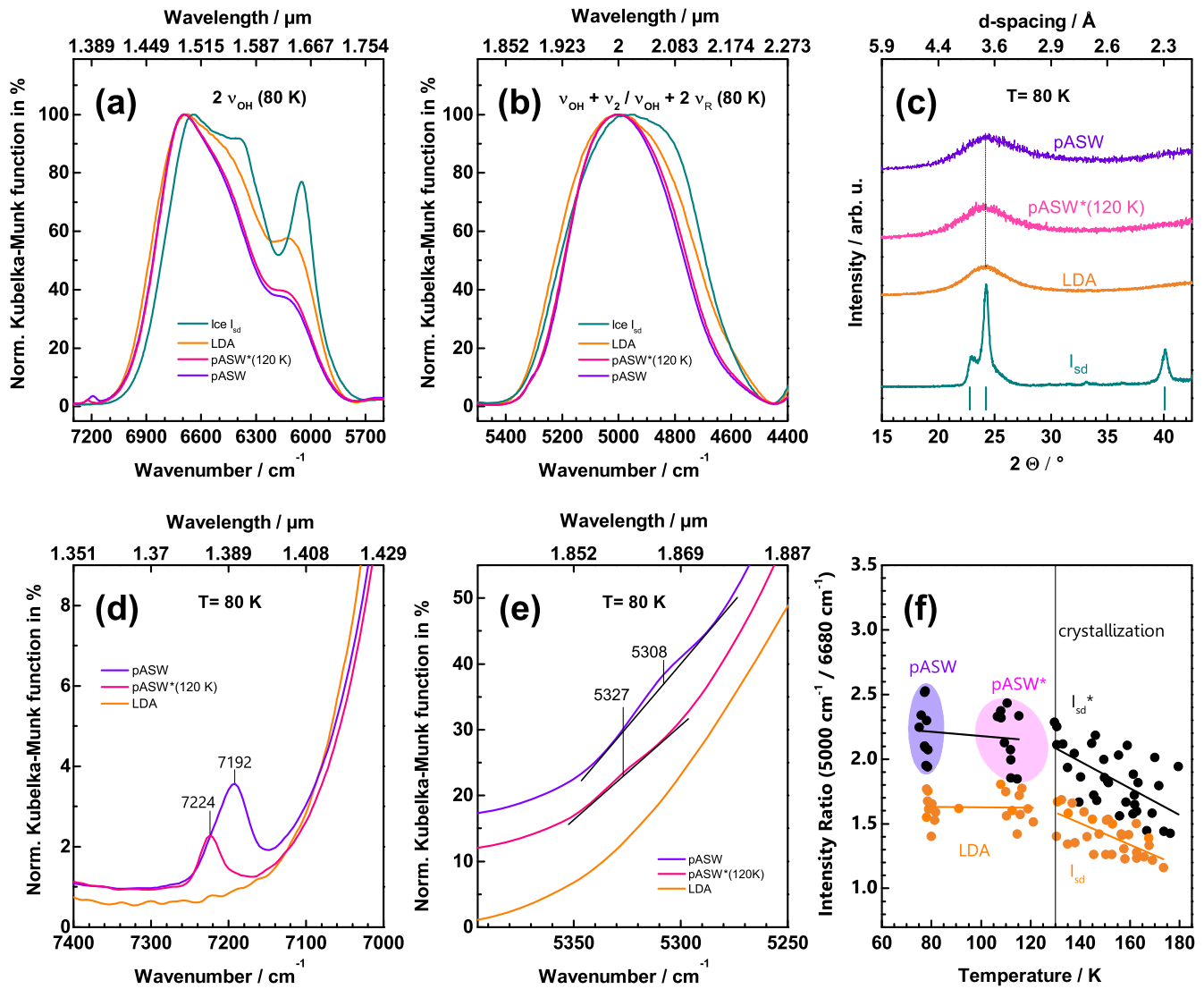
Figure 1. (a) $2\nu_{OH}$ and (b) 5000 band of pASW (purple), less porous "pASW*(120 K)" (pink), LDA (orange), and ice I_{sd} (turquoise). (c) PXRD of the poly(a)morphs shown in (a) and (b). Peak positions from literature (Dowell & Rinfret 1960; Winkel et al. 2011) are marked by vertical lines. (d) DB5 and (e) DB3 (Tribbett et al. 2021) of pASW and pASW*(120 K). The lines in (e) are offset for clarity. (f) Intensity ratio of the 5000 band relative to $2\nu_{OH}$ as a function of temperature of pASW and LDA. For fit parameters of trend lines, see Table B1.

and crystalline ice I_{sd}: (a) the first overtone band of the OH-stretching vibration $(2\nu_{OH})$ around $6600\,\mathrm{cm}^{-1}$ and (b) the combination band of OH-stretching and bending vibration as well as OH-stretching band with the first libration overtone $(\nu_{OH} + \nu_2/\nu_{OH} + 2\nu_R)$ around $5000\,\mathrm{cm}^{-1}$ (Table 1 and Figure A1 for full range). We quantify the spectral differences using peak positions and parameters characterizing peak broadness and band intensity ratios, such as position and intensity of the $2\nu_{OH}$ wing $\sim\!6050\,\mathrm{cm}^{-1}$, the full width at a third of the maximum (FWThM) of $2\nu_{OH}$, and the FWHM of the 5000 band (Table 2). Also, we define "red" and "blue" peak widths, "RPW" and "BPW," at 33% ($2\nu_{OH}$) and 50% (5000 band) of the height of the band maximum. ("Red"/"blue" means the difference between low/high-wavenumber edge and peak maximum in cm^{-1}; see Figure 2(a) for graphical representation).

Figure 1(a) highlights the $2\nu_{OH}$ shoulder of pASW and LDA. For LDA, this is a distinct subpeak at $6128\,\mathrm{cm}^{-1}$ and 57% relative intensity (Table 2). For pASW, we observe a much less

pronounced shoulder at $6171\,\mathrm{cm}^{-1}$ and only 39%. Also, the relative intensities at $6050\,\mathrm{cm}^{-1}$, which is a well-known marker band (Mastrapa et al. 2008), differ for pASW (31%) and LDA (52%) (Table 2). Moreover, the $2\nu_{OH}$ and 5000 bands are narrower for pASW compared to LDA (Figures 1(a) and (b)). These spectral differences cannot be explained by structural differences on the atomic scale, as deduced from PXRD (Figure 1(c)). pASW and LDA show the same, well-known halo peak maximum at $3.7\,\text{Å}$ $(24.3°)$ (Winkel et al. 2011). Instead, the spectral differences between pASW and LDA presumably arise from their distinct morphology, i.e., pore microstructure. To test this hypothesis, one batch of pASW was heated briefly to 120 K, in order to induce the collapse of some pores, and subsequently quenched to $\sim\!80$ K.

Confirming the hypothesis, the lower porosity becomes apparent in the NIR spectrum of "pASW*(120 K)": (i) by the increase of the 6171 shoulder, (ii) by the broadening of the $2\nu_{OH}$ and the 5000 band (Figures 1(a) and (b)), thereby showing a trend toward "LDA-like" features, and (iii) by the

Table 1
Band Positions of the Ices Studied Here (±10 cm^{-1})

Position of Band Maxima (cm^{-1})						
VHDA	HDA	LDA	pASW	Ice I$_c$	Ice I$_{sd}$	Ice I$_h$ (Tonauer et al. 2021)
$2\nu_{OH} + \nu_2$						
8180	8156	7936	7984	7870	7868	7888
				7660	7656	7656
$2\nu_{OH} + \nu_R$						
7400	7392					
DB 5 (Tribbett et al. 2021)						
7192 (7224[a])						
$2\nu_{OH}$						
6776	6752	6672	6692	6649	6648	6648
				6390	6390	6390
		6128	6171[b]	6060	6050	6049
$\nu_{OH} + \nu_2 + \nu_R$						
5604	5608	5600	5624	5620	5600	5600
DB 3 (Tribbett et al. 2021)						
5308 (5327[a])						
$\nu_{OH} + \nu_2/\nu_{OH} + 2\nu_R$						
5100	5092	5000	5000	4971	4956	4972

Notes.
[a] pASW*(120 K).
[b] Inflection point.

change of the position and intensity of the dangling bond (DB) bands (Figures 1(d) and (e)). For pASW and pASW*(120 K), we identify "DB5" (Tribbett et al. 2021) around $\sim$7200 cm^{-1} (Figure 1(d)). This feature was assigned to the first overtone of the dangling vibration of three-coordinated surface water molecules (DB2; Buch & Devlin 1991; Rowland et al. 1991). Furthermore, we observe "DB3" as a very weak shoulder around $\sim$5300 cm^{-1}, assigned to a combination of the dangling vibration of two-coordinated (DB1) and three-coordinated (DB2) surface water molecules with the bending mode (ν_2) (Hagen et al. 1981; Figure 1(e)). Comparing both pASW spectra, DB5 and DB3 are less intense and show a blueshift of $\sim$20–30 cm^{-1} for pASW*(120 K) relative to pASW (Table 1). Previous studies (Chaabouni et al. 2000; Raut et al. 2007; Fulvio et al. 2010) have shown a redshift of their spectral signatures upon binding of gas molecules with dangling bonds. During sample recovery, where the deposit on the cryoplate is taken out of the sample chamber and immersed under liquid nitrogen, we expect N$_2$ (and possibly O$_2$) from the liquid nitrogen bath to attach to DBs on the external surface of pASW, and therefore DB5 and DB3 to be redshifted relative to "free" pASW. Upon in situ heating of pASW to 120 K in the chamber, some pores already collapse, changing the morphology of the external surface. That is, there are less pores, less dangling bonds, and therefore less sites for external molecules to attach. Thus, we rationalize the blueshift and shrinking of DB5 and DB3 with the decrease of undercoordinated surface species, which is due to partial pore collapse in pASW*(120 K).

Furthermore, we identify the ratio between the 5000 and the $2\nu_{OH}$ bands to be an indication of porosity (Figure 1(f)). For pASW, the 5000 band shrinks (relative to $2\nu_{OH}$) with temperature, whereas this is not the case for LDA. We ascribe the different temperature dependence to morphology. At about 130 K, the temperature trend for both ices changes as a result of crystallization. After crystallization, the slope of the pASW and LDA trend lines is the same, but there is a y-offset between them (Table B1). This is likely a signature of pores remaining after crystallization, since pore sintering and crystallization may take place simultaneously at heating rates of $\sim$50 K min^{-1}. However, once the sample has fully crystallized, pore collapse ceases, and the remaining pores stay intact to much higher temperature. The difference in morphology between ice I$_{sd}$* (from pASW) and ice I$_{sd}$ (from LDA) remains up to temperatures of 180 K, probably even up to the melting or sublimation of the ice.

3.2. Density

We here report the first NIR study of amorphous ices of different densities, where their molecular structure is probed by PXRD (Figures 1(c) and A2). Evidently, there is a blueshift of the band positions for VHDA and HDA relative to LDA (Figures 2(a) and (b)). Also, the peak shape (broadness, subpeak/shoulder structure) clearly differs between them. While $2\nu_{OH}$ of LDA features a low-wavenumber wing at 6128 cm^{-1}, this feature is missing for HDA and VHDA. Remarkably, RPW of $2\nu_{OH}$ shows an excellent linear correlation with density, just like FWHM of the 5000 band (Figures 2(c) and (d), Table 2). In Figures 2(e) and (f), we follow the evolution of $2\nu_{OH}$ of HDA upon heating. We identify the $2\nu_{OH}$ position (Figure 2(e)) and the intensity at 6050 cm^{-1} (Figure 2(f)) to be reliable markers for monitoring phase transitions in ice. Even though the data points are somewhat scattered, the polyamorphic HDA $\rightarrow$ LDA transition and subsequent crystallization to ice I$_{sd}$ can be observed (Figures 2(e) and (f)).

These data shed new light on the interpretation of NIR spectra of ASW in literature. Mastrapa et al. conjecture (based on Jenniskens & Blake 1994) there are two kinds of amorphous deposits of different density, depending on whether deposition was conducted below or above 70 K (Mastrapa et al. 2008). While they observe no spectral changes with temperature at $T < 70$ K, above 70 K, they report an irreversible redshift of the $2\nu_{OH}$ and 5000 bands by 6 and 11 wavenumbers, respectively. They interpret this as a transition from a high-density to a low-density amorphous ice deposit. We rule out this interpretation based on (i) the shape of the $2\nu_{OH}$ shoulder (quantified by the intensity at 6050 cm^{-1}, Table 2), (ii) the peak position of the $2\nu_{OH}$ band, and (iii) the peak position of the 5000 band (Table 1). Note that a change from HDA to LDA would result in, e.g., a redshift of the $2\nu_{OH}$ maximum by 80 cm^{-1} and not only 6 cm^{-1}. Instead, we here put forward the following explanation: Mastrapa et al. in fact deposited low-density pASW at $<$70 K. This is evident from the strong DB5 and DB3 features (Figure 10 of Mastrapa et al. 2008). Their observed spectral changes are a result of changed morphology, likely due to pore clustering (Wu et al. 2010; Cazaux et al. 2015). Our interpretation is confirmed by neutron scattering, where a decrease of specific surface area and porosity of pASW between 20 and 100 K was shown (Gärtner et al. 2019).
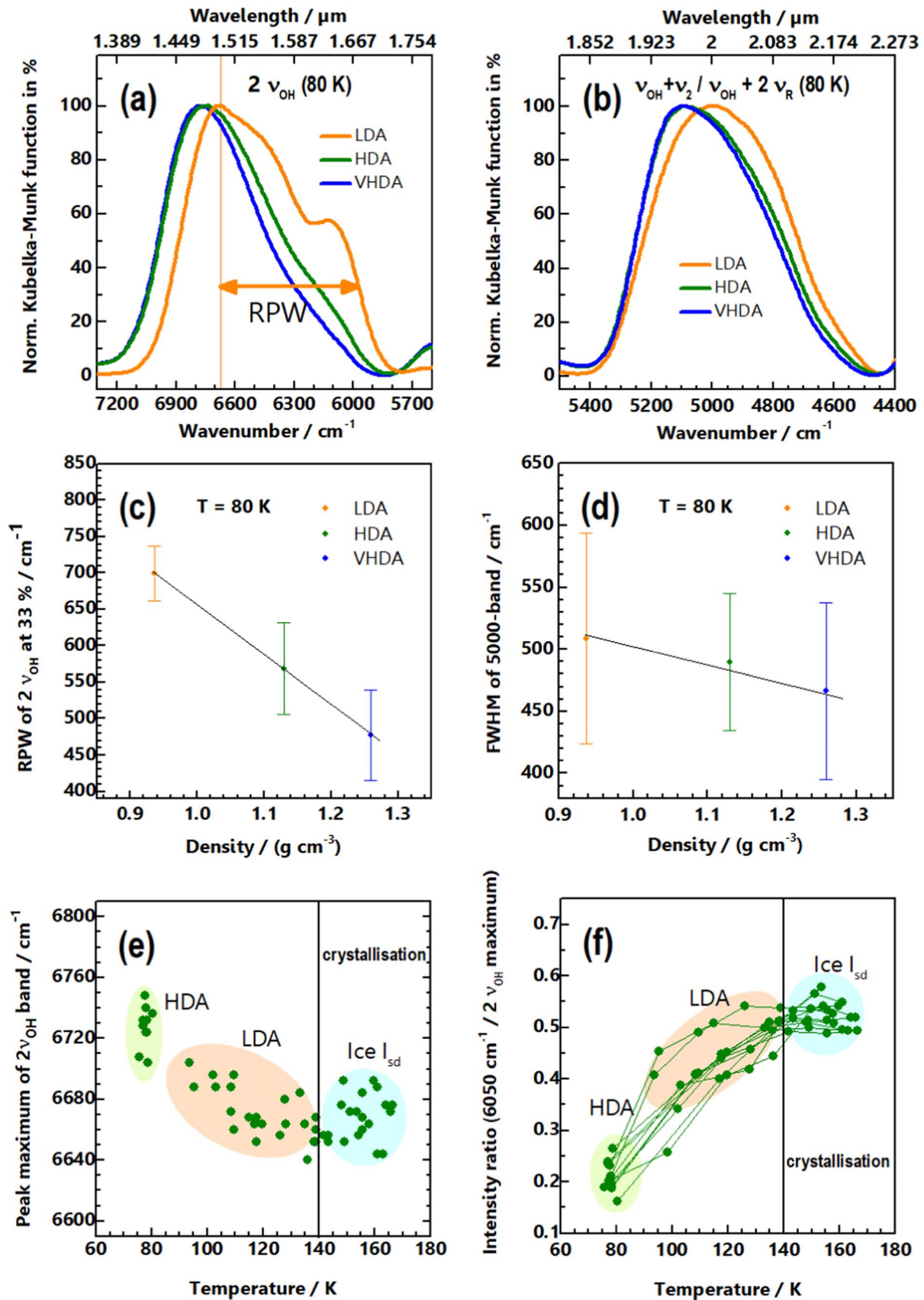
Figure 2. (a) $2\nu_{OH}$ and (b) 5000 band of LDA (orange), HDA (green), and VHDA (blue). (c) RPW of the $2\nu_{OH}$ band at 33% and (d) FWHM of the 5000 band vs. bulk density. (e) $2\nu_{OH}$ position and (f) intensity ratio (6050 cm^{-1} relative to $2\nu_{OH}$) upon heating HDA. For values, see Table 2.

Table 2
Parameters Characterizing the Peak Shape of $2\nu_{OH}$ and the Combinational Band $\nu_{OH} + \nu_2$, $\nu_{OH} + 2\nu_R$

	$2\nu_{OH}$					
	Position/cm^{-1}	Shoulder Intensity in %	Intensity at 6050 cm^{-1} in %	FWThM/cm^{-1}	Red Peak Width at 33% /cm^{-1}	Density/(g cm^{-1})
LDA	6672		52	961	699	0.937 (Loerting et al. 2011a)
	6128 shoulder	57				
pASW	6692		31	839	622	~0.4
	[a]6171 shoulder	39				
pASW* (120 K)	6692		33	859	641	>0.4, <0.93
	[a]6171 shoulder	41				
HDA	6752		19	850	568	1.13 (Loerting et al. 2011b)
VHDA	6776		11	742	477	1.26 (Loerting et al. 2011b)
IceI$_c$	6649					
	6390		67			
	6060 shoulder	67				
IceI$_{sd}$	6648					
	6390		77	914	697	0.943 (Loerting et al. 2011a)
	6050 shoulder	77				
Ice I$_h$	6648					
	6390		86	946	720	0.932 (Loerting et al. 2011a)
	6049 shoulder	87				
	$\nu_{OH} + \nu_2$, $\nu_{OH} + 2\nu_R$				
	Position/cm^{-1}	FWHM/cm^{-1}	Blue Peak Width at 50%/cm^{-1}	Red Peak Width at 50%/cm^{-1}	Intensity relative to $2\nu_{OH}$
LDA	5000	509	227	282	1.23
pASW	5004	424	186	237	2.39
pASW* (120 K)	5000	436	194	243	2.04
HDA	5092	490	162	328	1.33
VHDA	5100	466	152	314	1.64
Ice I$_c$	4971				
Ice I$_{sd}$	4956	516	252	264	1.48
Ice I$_h$	4972	566	262	304	1.32

Note.
[a] Inflection point.

3.3. Polytypism of Ice I

The NIR signatures of cubic ice I$_c$ and stacking-disordered ice I$_{sd}$ are compared with hexagonal ice I$_h$ (Tonauer et al. 2021; Figure 3). Since different stacking-disordered ices I$_{sd}$ differ in terms of the number of cubic/hexagonal layers, it is necessary to quantify their cubicity. Here, we define "calorimetric cubicity" as the ratio of ΔH at the transition to ice I$_h$ relative to the value observed for pure ice I$_c$ of -37.7 J mol^{-1} (Tonauer et al. 2023b). Note that the quantity "cubicity" introduced in Hansen et al. (2008) is obtained from neutron diffraction while we employ the exotherm obtained at the transition from cubic/stacking-disordered ice to hexagonal ice using calorimetry.

Bertie & Whalley (1964) were not able to detect any differences in the mid-infrared between polytypes of ice I in the 1960s. Carr et al. (2014) identified in their Raman study the broadening of the coupled ν_{OH} and ν_{OD} bands to be an indication for increased stacking-disorder. Pure cubic ice I$_c$ became experimentally accessible only in 2020 (del Rosso et al. 2020; Komatsu et al. 2020). A characterization of ice I$_c$ dynamics has been recently performed by ex situ Raman and neutron spectroscopic techniques (Celli et al. 2020; del Rosso et al. 2021). Thus, we here present the first spectroscopic study directly comparing spectra of ice I$_c$ with ice I$_h$ in the NIR range. Although the local coordination geometry in all ice I polytypes is essentially the same, our data reveal the distinctness between ices I$_h$, I$_{sd}$, and I$_c$ in the near-infrared region. We identify the following markers for cubicity: (i) the intensity of the 6050 cm^{-1} subpeak, which is low for ice I$_c$ (67%) and increases with decreasing calorimetric cubicity to 77% (ice I$_{sd}$) and 87% (ice I$_h$) (Figures 3(a) and (c), Table 2). (ii) The position of the feature at 6050 cm^{-1} for ice I$_h$, which is blueshifted to 6060 cm^{-1} for ice I$_c$ (Table 1). (iii) The FWHM of the 5000 band, which decreases with increasing calorimetric cubicity in a linear trend (Figures 3(b) and (d), Table 2). That is, stacking-disordered ice, containing both cubic and hexagonal stacked layers to a similar extent (42% calorimetric cubicity), shows spectra in between, with an excellent linear correlation with cubicity.
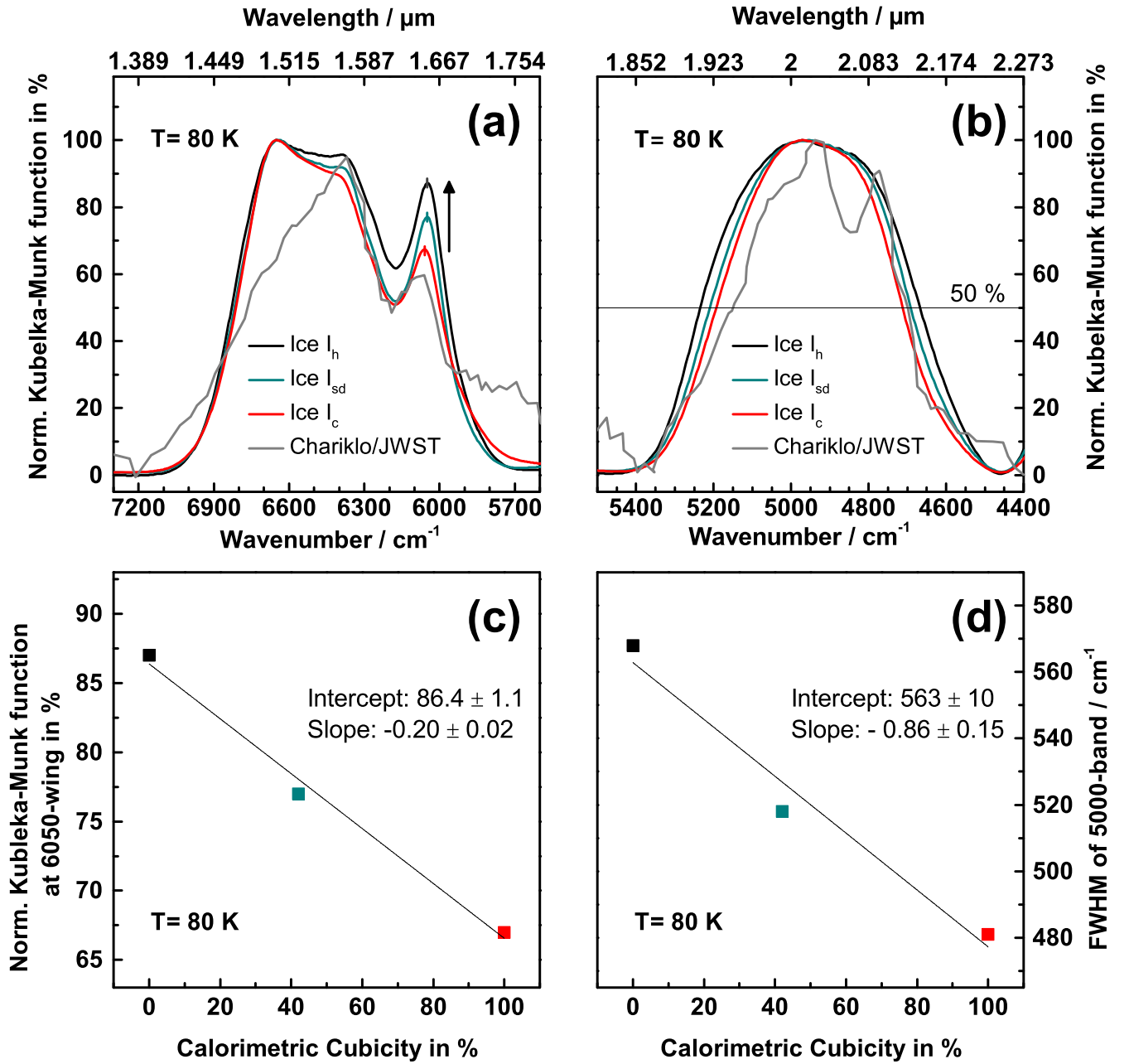
Figure 3. (a) $2\nu_{OH}$ and (b) 5000 band of ice I_c (red), ice I_{sd} (turquoise), and ice I_h (dark gray; Tonauer et al. 2021) in comparison with remotely collected data from the centaur 10199 Chariklo that orbits the Sun between Saturn and Uranus. Chariklo/JWST data were extracted from the graphic "Centaur 10199 Chariklo: Surface Composition; NIRSpec PRISM (Pinilla-Alonso et al. 2023). (c) Intensity at the 6050 wing (highlighted by an upward-pointing arrow in (a)) and (d) FWHM of the 5000 band (marked by a horizontal line in (b)) vs. calorimetric cubicity.

While we utilize the intensity of the $6050\,\mathrm{cm}^{-1}$ subpeak relative to the $6648\,\mathrm{cm}^{-1}$ position, other reference positions (e.g., $6390\,\mathrm{cm}^{-1}$; Table 1) should be taken into account when comparing our laboratory data with remotely sensed spectra from space. This becomes evident upon inspection of a recently collected spectrum (2022 October 31) of the outer Solar System object 10199 Chariklo (Braga-Ribas et al. 2014), using the NIRSpec PRISM instrumentation on JWST (Pinilla-Alonso et al. 2023), depicted in Figures 3(a) and (b) (see Section 2 for conversion of spectral data). Chariklo is a centaur originating from the Kuiper Belt, orbiting the Sun between Uranus and Saturn. Just like Saturn, it features rings, where the presence of water ice was identified. The temperatures ~60–90 K for the Chariklo system (Lellouch et al. 2017) allow for direct comparison with our lab spectra collected at 80 K. While temperature-dependent spectra are the object of future work, it is clear from our present work that the mere presence of the "$6050\,\mathrm{cm}^{-1}/1.65\,\mu\mathrm{m}$" wing is not a sufficient criterion to identify crystalline ice. Also, LDA shows a similar wing feature of the $2\nu_{OH}$ (Figure 2(a)). That is, the practice of taking observations of the wing as proof for crystalline H_2O ice (Jewitt & Luu 2004) needs to be refined. More spectral markers, e.g., peak broadness (RPW) and intensity ratios, should be considered for clear distinction between (different) crystalline and amorphous ices.

4. Astrophysical Implications

The present results clearly suggest that the near-infrared spectrum above $4000\,\mathrm{cm}^{-1}$/below $2.5\,\mu\mathrm{m}$ contains important

marker bands relevant for remote sensing of different H_2O ices. In order to test the applicability for astronomical observations, we utilized the JWST Exposure Time Calculator (Pontoppidan et al. 2016) to estimate exposure times necessary for observing the first overtone band of the OH-stretching vibration $2\nu_{OH}$ ($\sim$6600 cm^{-1}/1.5 μm) using JWST NIRSpec. As mentioned before, the diffuse reflectance NIR spectroscopy technique does not allow for extraction of absolute values for absorptivities, but absorptivities for hexagonal ice are well known over a wide spectral range (Hudgins et al. 1993; Warren & Brandt 2008). For the exposure time estimates, we consider fluxes as they were observed toward the embedded protostar W33A (Capps et al. 1978; Gibb et al. 2000; de Wit et al. 2007), a massive young stellar object and a common target for ice absorption features (Tribbett et al. 2021). Gibb et al. show the flux spectrum of W33A in their Figure 2 between 2.5 and 6 μm, where the 3.3 μm wing shows a depth of $\sim$3800 mJy. Since the spectral range below 2.5 μm is not covered in their measurement, we have to estimate a value for the flux at 1.5 μm. We use the ratio of the known literature absorptivity values (Warren & Brandt 2008) at 3.3 μm and 1.5 μm to assume a flux value at 1.5 μm relative to the 3800 mJy deep 3.3 μm band. Accordingly, we relate the 3800 mJy deep 3.3 μm wing to the literature value of (linear) absorptivity of $\sim$12,760 cm^{-1} and estimate the 1.5 μm feature (showing an absorptivity of 45 cm^{-1}; Warren & Brandt 2008) to show a 14 mJy deep band. Similarly to the calculation of Tribbett et al. (2021), we estimate exposure times using NIRSpec at fixed slit observation mode and pick the G140H/F100LP disperser-filter combination with a resolving power of 2700, covering the first overtone band (0.97–1.82 μm). After 42 integrations (with six groups per integration) using the NRS readout pattern and a total exposure time of 1636.76 s ($\sim$27 minutes), we find signal-to-noise ratios (S/Ns) $\sim$ 250. In a tentative attempt to assess this result, we compare it with the exposure time calculation of Tribbett et al. and find agreement. They considered the dangling bond features DB3 ($\sim$5300 cm^{-1}) and DB5 ($\sim$7200 cm^{-1}), which are about $\sim$100 times weaker than the $2\nu_{OH}$ band at 1.5 μm/6600 cm^{-1} (Figures 2(d), (e)). They report an exposure time estimate of 4.5 hr ($=$16,200 s) for S/Ns above 3. In other words, by considering a roughly $\sim$100 times stronger band than Tribbett et al., a tenth of their exposure time is sufficient, yielding a 1–2 orders of magnitude higher S/N. Given the result of our exposure time estimate, we consider the near-infrared range (below 2.5 μm/above 4000 cm^{-1}) to be a valuable diagnostic spectral range for H_2O ices in astronomical environments observable by JWST.

5. Conclusions

We present near-infrared spectra (backed by powder X-ray diffraction) of astronomically relevant amorphous and crystalline H_2O ice analogs at $\sim$80–180 K. We disentangle the effects of porosity and density on the spectra of different amorphous ices (pASW, collapsed ASW, LDA, HDA, and VHDA). In addition to dangling bonds, we show that porosity manifests in (i) the position and intensity of the $2\nu_{OH}$ shoulder, (ii) the broadness of the $2\nu_{OH}$ and 5000 band, and (iii) the intensity of the 5000 band relative to $2\nu_{OH}$. For density, the broadness of the $2\nu_{OH}$ shoulder, and more specifically, the red peak width (RPW), is a strong indicator. Combining these results, the long-standing hypothesis that ASW deposited below 70 K represents a high-density form of amorphous ice (Jenniskens & Blake 1994; Mastrapa et al. 2008) can be ruled out. Finally, we demonstrate that hexagonal ice and cubic ice can be differentiated by near-infrared spectroscopy, thus refuting the long-standing belief that their IR spectra need to be identical because of the identical local coordination (Bertie & Whalley 1964). So far, low-density ice observed on celestial bodies has only been classified as "crystalline" or "amorphous" ice (Filacchione et al. 2016; Robidel et al. 2020; Berdis et al. 2022). The present study goes beyond previous work in that it allows for a remote, NIR spectroscopic distinction of ice I polytypes (ice I_h, ice I_c, and ice I_{sd}) and to disentangle porosity and bulk density of amorphous ices. This will be of relevance for understanding icy moons, such as Europa, Ganymede, or Enceladus, Saturn rings, cometary ices, and possibly even interstellar dust grains covered in ices. Our lab study offers new reference spectra for modeling the observations of JWST (e.g., the recent one of centaur 10199 Chariklo) and future observations of JUICE, facilitating access to porosity and cubicity of interstellar objects. Ultimately, this will be important for the search for habitability in space (Ligier et al. 2019).

Appendix A
Sample Characterization Methods

We here show supporting information on full-range NIR spectra (Figure A1), powder X-ray diffraction (Figure A2), and differential scanning calorimetry (Figure A3).
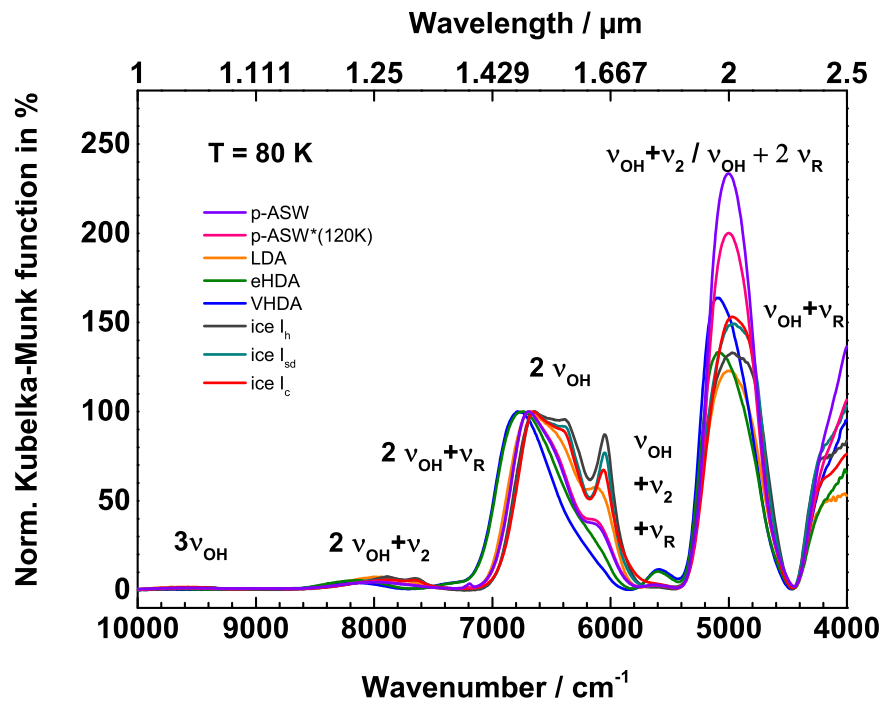
Figure A1. Full-range spectra (10,000–4000 cm^{-1}/1–2.5 μm) of all ices scrutinized in the present study; the spectrum of ice I$_h$ is taken from Tonauer et al. (2021). For comparison, they are aligned at the maximum of the 2ν_{OH} band.
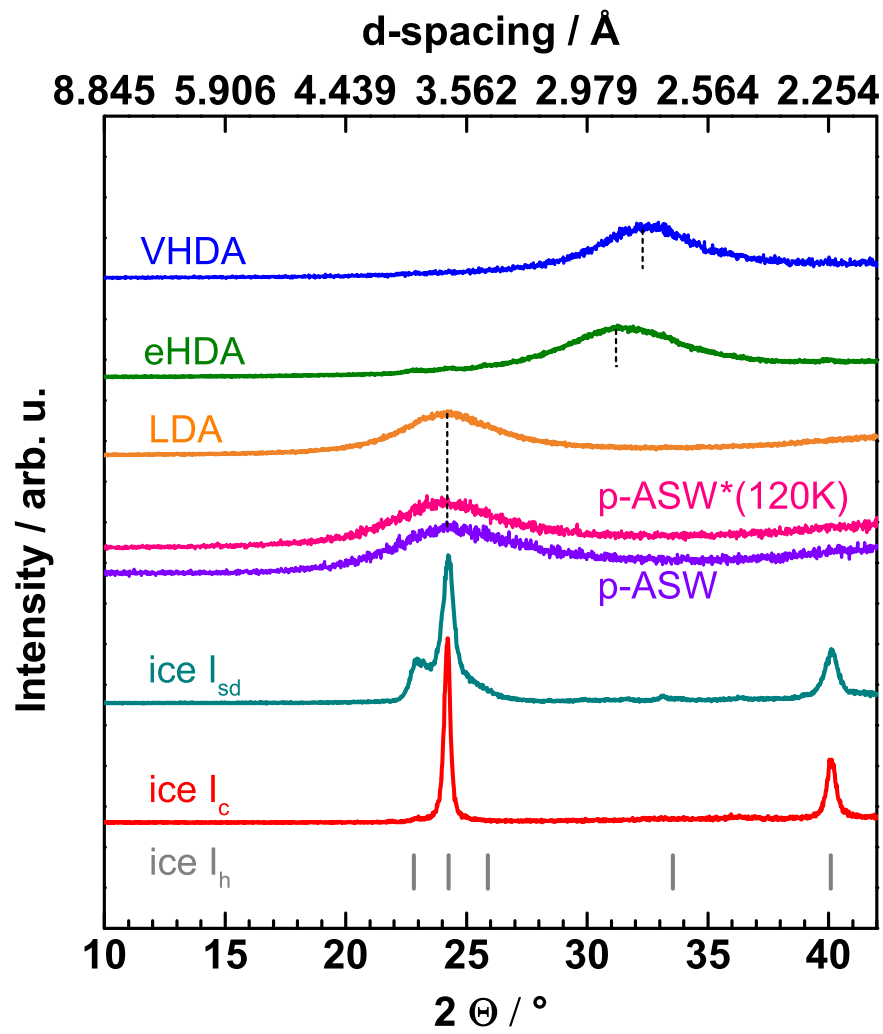
Figure A2. Powder X-ray diffractograms of all ices considered in the present study (one representative scan for each form of ice is shown). Literature values of positions of broad halo peaks for amorphous ices and sharp Bragg peaks for ice I_h are marked by vertical lines (Dowell & Rinfret 1960; Winkel et al. 2011).
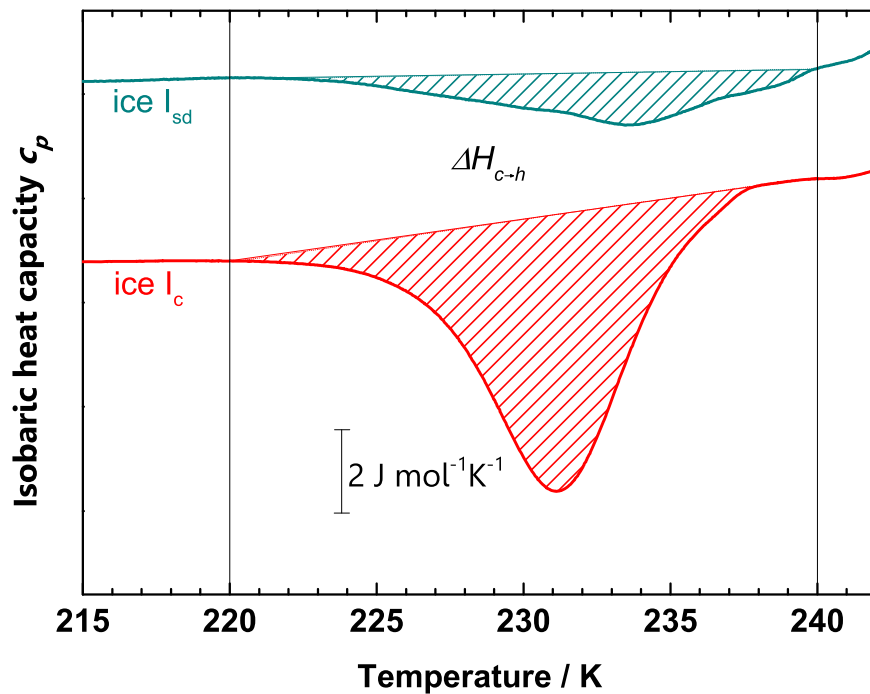
Figure A3. Examples of typical calorimetry scans for ice I_{sd} (turquoise) and ice I_c (red) upon heating at 30 K min^{-1}. The respective integrals of the transition exotherms ($\Delta H_{c \rightarrow h}$) considered for determination of calorimetric cubicity are marked by dashed fill. For each of the four batches of ice I_{sd} considered, at least two scans were recorded. Based on these thermograms, calorimetric cubicity of each batch was calculated. For the sum spectrum of ice I_{sd} (Figures 3(a), (b), A1), calorimetric cubicity was averaged (weighted by the number of single spectra collected of each batch), resulting in a value of 42% calorimetric cubicity.

Appendix B
Spectral Changes upon Heating pASW and LDA

Table B1 includes the fit parameters of the trend lines describing the intensity ratios between the 5000 band and the $2\nu_{OH}$ band upon heating (80–180 K) for ASW and LDA, respectively, shown in Figure 1(f).

Table B1
Fit Parameters of Trend Lines of Figure 1(f)

ASW, Linear Fit	80–120 K	130–180 K
Intercept	2.36 ± 0.27	3.4 ± 0.4
Slope	$-2E\text{-}03 \pm 3E\text{-}03$	$-1.0E\text{-}02 \pm 2E\text{-}03$
LDA, Linear Fit	80–120 K	130–180 K
Intercept	1.63 ± 0.14	2.67 ± 0.27
Slope	$1.2E\text{-}05 \pm 1E\text{-}03$	$-8E\text{-}03 \pm 2E\text{-}03$

Appendix C
Raw Spectra

Raw diffuse reflectance (single) spectra (lines 1–5) of the poly(a)morphs LDA (Table C1), HDA (Table C2), VHDA (Table C3), pASW (Table C4), pASW*(120 K) (Table C5), ice I_{sd} (Table C6) and ice I_c (Table C7), shown in Figures 1(a), 1(b) 2(a), 2(b) 3(a), 3(b), and A1.

Table C1
Single Raw Diffuse Reflectance Spectra of LDA measured at $\sim$ 80 K

Wavenumber	LDA.01	LDA.02	LDA.03	LDA.04	…	LDA.27
4000	0.04486	0.20867	0.0246	0.02051		0.36476
4004	0.04642	0.20854	0.02456	0.02054		0.36488
4008	0.04742	0.20822	0.0245	0.02059		0.36499
4012	0.04757	0.20787	0.02453	0.02068		0.3651
4016	0.04723	0.20789	0.02474	0.02079		0.36524
…	…	…	…	…		…

(This table is available in its entirety in machine-readable form in the online article.)

Table C2
Single Raw Diffuse Reflectance Spectra of HDA measured at $\sim$ 80 K

Wavenumber	HDA.01	HDA.02	HDA.03	HDA.04	…	HDA.24
4000	0.02239	0.04152	0.02321	0.0209		0.30151
4004	0.02196	0.04151	0.02316	0.02096		0.30085
4008	0.02129	0.04141	0.02315	0.02097		0.30031
4012	0.02068	0.04126	0.02316	0.02087		0.30063
4016	0.02055	0.04108	0.0232	0.02071		0.30167
…	…	…	…	…		…

(This table is available in its entirety in machine-readable form in the online article.)

Table C3
Single Raw Diffuse Reflectance Spectra of VHDA measured at $\sim$ 80 K

Wavenumber	VHDA.01	VHDA.02	VHDA.03	VHDA.04	…	VHDA.25
4000	0.02508	0.03014	0.01955	0.01975		0.06262
4004	0.02506	0.03035	0.01974	0.01975		0.06204
4008	0.02506	0.03049	0.01999	0.01934		0.06171
4012	0.0251	0.0305	0.02014	0.019		0.06232
4016	0.02518	0.03039	0.02018	0.01904		0.06354
…	…	…	…	…		…

(This table is available in its entirety in machine-readable form in the online article.)

Table C4
Single Raw Diffuse Reflectance Spectra of pASW measured at $\sim$ 80 K

Wavenumber	pASW.01	pASW.02	pASW.03	pASW.04	…	pASW.20
4000	0.19324	0.0737	0.30225	0.26409		0.23049
4004	0.19368	0.07387	0.30245	0.26467		0.23038
4008	0.19422	0.07409	0.30293	0.26535		0.23036
4012	0.19483	0.07434	0.30363	0.26614		0.23047
4016	0.19548	0.07465	0.30447	0.26702		0.23068
…	…	…	…	…		…

(This table is available in its entirety in machine-readable form in the online article.)

Table C5
Single Raw Diffuse Reflectance Spectra of pASW*(120 K) measured at ~ 80 K

Wavenumber	pASW120K.01	pASW120K.02	pASW120K.03	pASW120K.04	…	pASW120K.10
4000	0.25942	0.26115	0.15302	0.17818		0.37003
4004	0.25994	0.26173	0.15328	0.17852		0.3702
4008	0.26056	0.26243	0.15363	0.17892		0.37041
4012	0.26129	0.26326	0.15406	0.17938		0.37068
4016	0.26212	0.26421	0.15456	0.17993		0.37111
…	…	…	…	…		…

(This table is available in its entirety in machine-readable form in the online article.)

Table C6
Single Raw Diffuse Reflectance Spectra of ice I_{sd} measured at ~ 80 K

Wavenumber	Isd.01	Isd.02	Isd.03	Isd.04	…	Isd.38
4000	0.1015	0.02774	0.02775	0.02558		0.02431
4004	0.10045	0.02745	0.02794	0.02555		0.02505
4008	0.09877	0.02724	0.02816	0.02546		0.02543
4012	0.09618	0.02717	0.02843	0.02553		0.02541
4016	0.09291	0.02725	0.02878	0.02588		0.02529
…	…	…	…	…		…

(This table is available in its entirety in machine-readable form in the online article.)

Table C7
Single Raw Diffuse Reflectance Spectra of Ice I_c measured at ~ 80 K

Wavenumber	Ic.01	Ic.02	Ic.03	Ic.04	…	Ic.10
4000	0.12775	0.23927	0.38099	0.16911		0.40077
4004	0.12794	0.23942	0.3806	0.16933		0.40072
4008	0.12819	0.23961	0.38031	0.1696		0.40077
4012	0.12846	0.23984	0.3801	0.16991		0.40091
4016	0.12874	0.24012	0.37995	0.17026		0.40112
…	…	…	…	…		…

(This table is available in its entirety in machine-readable form in the online article.)

ORCID iDs

Christina M. Tonauer ⑩ https://orcid.org/0000-0001-6859-5344
Eva-Maria Köck ⑩ https://orcid.org/0000-0002-4642-8315
Raphael Henn ⑩ https://orcid.org/0000-0001-9091-7223
Josef N. Stern ⑩ https://orcid.org/0000-0003-2171-7329
Leonardo del Rosso ⑩ https://orcid.org/0000-0002-7134-4121
Milva Celli ⑩ https://orcid.org/0000-0002-0537-6029
Christoph Kappacher ⑩ https://orcid.org/0000-0003-0687-5732
Christian G. Kirchler ⑩ https://orcid.org/0000-0003-0964-6820
Christian W. Huck ⑩ https://orcid.org/0000-0002-6272-3242
Thomas Loerting ⑩ https://orcid.org/0000-0001-6694-3843

References

Alan Stern, S. 2003, Natur, 424, 639
Baragiola, R. A. 2003, P&SS, 51, 953
Bar-Nun, A., Dror, J., Kochavi, E., & Laufer, D. 1987, PhRvB, 35, 2427
Berdis, J. R., Murphy, J. R., & Chanover, N. J. 2022, PSJ, 3, 36
Bertie, J. E., & Whalley, E. 1964, JChPh, 40, 1637
Bland, M. T., Singer, K. N., McKinnon, W. B., & Schenk, P. M. 2012, GeoRL, 39, 2012GL052736
Bossa, J.-B., Isokoski, K., De Valois, M. S., & Linnartz, H. 2012, A&A, 545, A82
Bossa, J.-B., Maté, B., Fransen, C., et al. 2015, ApJ, 814, 47
Braga-Ribas, F., Sicardy, B., Ortiz, J. L., et al. 2014, Natur, 508, 72
Buch, V., & Devlin, J. P. 1991, JChPh, 94, 4091
Burke, D. J., & Brown, W. A. 2010, PCCP, 12, 5947
Burton, E. F., & Oliver, W. F. 1935, Natur, 135, 505
Capps, R., Gillett, F., & Knacke, R. 1978, ApJ, 226, 863
Carr, T. H. G., Shephard, J. J., & Salzmann, C. G. 2014, JPCL, 5, 2469
Cazaux, S., Bossa, J.-B., Linnartz, H., & Tielens, A. G. G. M. 2015, A&A, 573, A16
Celli, M., Ulivi, L., & del Rosso, L. 2020, JPCC, 124, 17135
Chaabouni, H., Schriver-Mazzuoli, L., & Schriver, A. 2000, JPCA, 104, 6962
Dartois, E., Ding, J. J., de Barros, A. L. F., et al. 2013, A&A, 557, A97
de Wit, W. J., Hoare, M. G., Oudmaijer, R. D., & Mottram, J. C. 2007, ApJ, 671, L169
del Rosso, L., Celli, M., Colognesi, D., et al. 2021, JPCC, 125, 23533
del Rosso, L., Celli, M., Grazzi, F., et al. 2020, NatMa, 19, 663
Dohnálek, Z., Kimmel, G. A., Ayotte, P., Smith, R. S., & Kay, B. D. 2003, JChPh, 118, 364
Dowell, L. G., & Rinfret, A. P. 1960, Natur, 188, 1144
Filacchione, G., De Sanctis, M. C., Capaccioni, F., et al. 2016, Natur, 529, 368
Fulvio, D., Guglielmino, S., Favone, T., & Palumbo, M. E. 2010, A&A, 511, A62
Gärtner, S., Headen, T. F., Youngs, T. G. A., et al. 2019, in IAU Proc. 350, Laboratory Astrophysics: From Observations to Interpretation (Cambridge: Cambridge Univ. Press), 368

Gibb, E. L., Whittet, D. C. B., Schutte, W. A., et al. 2000, ApJ, 536, 347
Grundy, W. M., & Schmitt, B. 1998, JGRE, 103, 25809
Hagen, W., Tielens, A. G. G. M., & Greenberg, J. M. 1981, CP, 56, 367
Hallbrucker, A., & Mayer, E. 1991, Icar, 90, 176
Hansen, T. C., Koza, M. M., & Kuhs, W. F. 2008, JPCM, 20, 285104
Harada, N., Herbst, E., & Wakelam, V. 2010, ApJ, 721, 1570
Harada, N., Herbst, E., & Wakelam, V. 2012, ApJ, 756, 104
Hudgins, D. M., Sandford, S. A., Allamandola, L. J., & Tielens, A. G. G. M. 1993, ApJS, 86, 713
Isokoski, K., Bossa, J.-B., Triemstra, T., & Linnartz, H. 2014, PCCP, 16, 3456
Jenniskens, P., & Blake, D. 1994, Sci, 265, 753
Jewitt, D. C., & Luu, J. 2004, Natur, 432, 731
Kargel, J. S., & Pozio, S. 1996, Icar, 119, 385
Karina, A., Eklund, T., Tonauer, C. M., et al. 2022, JPCL, 13, 7965
Kimmel, G. A., Stevenson, K. P., Dohnálek, Z., Smith, R. S., & Kay, B. D. 2001, JChPh, 114, 5284
Klinger, J. 1985, Ices in the Solar System (Dordrecht: Kluwer)
Kolesnikov, A. I., Li, J.-C., Dong, S., et al. 1997, PhRvL, 79, 1869
Komatsu, K., Machida, S., Noritake, F., et al. 2020, NatCo, 11, 464
Kubelka, P., & Munk, F. 1931, Fuer. Tekn. Phys., 12, 593
Kuhs, W. F., Sippel, C., Falenty, A., & Hansen, T. C. 2012, PNAS, 109, 21259
Lellouch, E., Moreno, R., Müller, T., et al. 2017, A&A, 608, A45
Leto, G., Gomis, O., & Strazzulla, G. 2005, MSAIS, https://articles.adsabs.harvard.edu/pdf/, 6, 57
Ligier, N., Paranicas, C., Carter, J., et al. 2019, Icar, 333, 496
Lin, C., Smith, J. S., Sinogeikin, S. V., & Shen, G. 2018, PNAS, 115, 2010
Loerting, T., Bauer, M., Kohl, I., et al. 2011a, JPCB, 115, 14167
Loerting, T., Salzmann, C., Kohl, I., Mayer, E., & Hallbrucker, A. 2001, PCCP, 3, 5355
Loerting, T., Winkel, K., Seidl, M., et al. 2011b, PCCP, 13, 8783
Malkin, T. L., Murray, B. J., Salzmann, C. G., et al. 2015, PCCP, 17, 60
Mastrapa, R., Bernstein, M., Sandford, S., et al. 2008, Icar, 197, 307
Mayer, E., & Pletzer, R. 1984, JChPh, 80, 2939
Mayer, E., & Pletzer, R. 1986, Natur, 319, 298
Mayer, E., & Pletzer, R. 1987, JPhyC, 48, C1–581
McBride, C., Vega, C., Sanz, E., & Abascal, J. L. F. 2004, JChPh, 121, 11907
McClure, M. K., Rocha, W. R. M., Pontoppidan, K. M., et al. 2023, NatAs, 7, 431

Mejía, C., de Barros, A. L. F., Seperuelo Duarte, E., et al. 2015, Icar, 250, 222
Mishima, O., Calvert, L. D., & Whalley, E. 1984, Natur, 310, 393
Mishima, O., Calvert, L. D., & Whalley, E. 1985, Natur, 314, 76
Mitterdorfer, C., Bauer, M., Youngs, T. G. A., et al. 2014, PCCP, 16, 16013
Öberg, K. I. 2016, ChRv, 116, 9631
Palumbo, M. E. 2006, A&A, 453, 903
Pinilla-Alonso, N., Wong, I., & Licandro, J. 2023, https://webbtelescope.org/contents/media/images/01GQJ89HXD39F20PSXS2KKKREB
Pontoppidan, K. M., Pickering, T. E., Laidler, V. G., et al. 2016, Proc. SPIE, 9910, 44
Porco, C. C., Helfenstein, P., Thomas, P. C., et al. 2006, Sci, 311, 1393
Raut, U., Famá, M., Teolis, B. D., & Baragiola, R. A. 2007, JChPh, 127, 204713
Robidel, R., Le Mouélic, S., Tobie, G., et al. 2020, Icar, 349, 113848
Rocha, W. R. M., Rachid, M. G., Olsthoorn, B., et al. 2022, A&A, 668, A63
Rowland, B., Fisher, M., & Devlin, J. P. 1991, JChPh, 95, 1378
Schmitt, B., Quirico, E., Trotta, F., & Grundy, W. M. 1998, in Solar System Ices, ed. B. Schmitt, C. De Bergh, & M. Festou, Vol. 227 (Dordrecht: Springer), 199
Terwisscha Van Scheltinga, J., Marcandalli, G., McClure, M. K., Hogerheijde, M. R., & Linnartz, H. 2021, A&A, 651, A95
Tonauer, C. M., Fidler, L.-R., Giebelmann, J., Yamashita, K., & Loerting, T. 2023a, JChPh, 158, 141001
Tonauer, C. M., Köck, E.-M., Gasser, T. M., et al. 2021, JPCA, 125, 1062
Tonauer, C. M., Seidl-Nigsch, M., & Loerting, T. 2018, JPCM, 30, 034002
Tonauer, C. M., Yamashita, K., del Rosso, L., Celli, M., & Loerting, T. 2023b, JPCL, 14, 5055
Torrent, J., & Barrón, V. 2015, in SSSA Book Series, ed. A. L. Ulery & L. Richard Drees (Madison, WI: American Society of Agronomy and Soil Science Society of America), 367, http://doi.wiley.com/10.2136/sssabookser5.5.c13
Tribbett, P. D., Tegler, S. C., & Loeffler, M. J. 2021, ApJ, 915, 40
Van Dishoeck, E. F., Herbst, E., & Neufeld, D. A. 2013, ChRv, 113, 9043
Warren, S. G., & Brandt, R. E. 2008, JGRD, 113, D14220
Winkel, K., Mayer, E., & Loerting, T. 2011, JPCB, 115, 14141
Wu, Y. C., Kallis, A., Jiang, J., & Coleman, P. G. 2010, PhRvL, 105, 066103